Biomineralization of a titanium-modified hydroxyapatite semiconductor on conductive wool fibers.

Alessio Adamiano [a] *, Nicola Sangiorgi [a], Simone Sprio [a], Andrea Ruffini [a], Monica Sandri [a], Alessandra Sanson [a], Pierre Gras [b,f], David Grossin [b], Christine Francès [f], Konstantinos Chatzipanagis [c], Matthew Bilton [c], Bartosz Marzec [d], Alessio Varesano [e], Fiona Meldrum [d], Roland Kröger [c] and Anna Tampieri [a]

[a] *Institute of Science and Technology for Ceramics (ISTEC), National Research Council (CNR), Via Granarolo 64, 48018 Faenza, Italy*

[b] *CIRIMAT, Université de Toulouse, CNRS/INPT/UPS UMR 5085, Ensiacet, 4 allée Emile Monso, 31030 Toulouse Cedex 4, France.*

[c] *Department of Physics, University of York, York YO10 5DD, U.K.*

[d] *School of Chemistry, University of Leeds, Woodhouse Lane, Leeds LS2 9JT, U.K.*

[e] *CNR-ISMAC, Institute for Macromolecular Studies, C.so G. Pella 16, 13900 Biella, Italy*

[f] *Laboratoire de Génie Chimique, Université de Toulouse, CNRS/INPT/UPS UMR 5503, Ensiacet, 4 allée Emile Monso, 31432 Toulouse Cedex 4, France.*

Author for correspondence: Dr. Alessio Adamiano

Institute of Science and Technology for Ceramics (ISTEC)
National Research Council (CNR),
Via Granarolo 64, 48018 Faenza (RA), Italy.
E-mail: alessio.adamiano@istec.cnr.it
Tel: +39 0546699761

Abstract

Metal ions are frequently incorporated into crystalline materials to improve their electrochemical properties and to confer new physicochemical properties. Naturally-occurring phosphate apatite, which is formed geologically and in biomineralization processes, has extensive potential applications and is therefore an attractive functional material. In this study, we generate a novel building block for flexible optoelectronics using bio-inspired methods to deposit a layer of photoactive titanium-modified hydroxyapatite (TiHA) nanoparticles (NPs) on conductive polypyrrole(PPy)-coated wool yarns. The titanium concentration in the reaction solution was varied between 8-50 mol% with respect to the phosphorous, which led to titanate ions replacing phosphate in the hydroxyapatite lattice at levels up to 17 mol%. PPy was separately deposited on wool yarns by oxidative polymerization, using two dopants: (i) antraquinone-2-sulfonic acid to increase the conductivity of the PPy layer and (ii) pyroglutamic acid, to reduce the resistivity of the wool yarns and to promote the heterogeneous nucleation of the TiHA NPs. A specific titanium concentration (25 mol% wrt P) was used to endow the TiHA NPs on the PPy-coated fibers with a desirable band gap value of 3.68 eV, and a specific surface area of 146 m^2/g. This is the first time that a thin film of a wide-band gap semiconductor has been deposited on natural fibers to create a fiber-based building block that can be used to manufacture flexible electronic devices.

Keywords: titanium doping; calcium phosphate nanoparticles; wide band gap semiconductor; flexible electronics; biomineralization

1.Introduction

The demand for high performance materials for flexible electronics has motivated the search for building blocks which exhibit specific properties including favourable band gaps, charge carrier mobility, light emission efficiency and quantum yield to construct new electronic devices such as organic and hybrid electronic materials.[1] Doping with metal ions is an effective route for tuning the electronic properties of functional materials, improving their performance and endowing them with new electrochemical properties.[2,3] Cerium,[4] tin [5] and scandium [6] have been widely used to improve the efficiency of TiO_2-based semiconductors used in dye sensitized solar cells (DSCs), where their incorporation facilitates electron injection by tuning the photoanode band gap and increasing the solar energy conversion efficiency.

Metal ions can be also incorporated within phases that do not normally exhibit valuable physico-chemical characteristics to create new materials that are well suited to optoelectronic applications. An excellent example is provided by pure hydroxyapatite (HA, $Ca_{10}(PO_4)_6(OH)_2$) whose 6.0 eV can be lowered by titanium incorporation to values nearing those of wide band gap semiconductors.[7] The versatility of this material - that finds numerous industrial applications ranging from water remediation to catalysis [8-10] is fostered by the readiness with which its lattice can be doped to various extents with monovalent to tetravalent anions and cations, [11] to generate HA with tailored properties [12,13]

Doped HA has also attracted considerable attention thanks to its favorable electrochemical properties. Liu *et al.* [14] reported an increase in the UV absorption of HA nanoparticles (NPs) doped with Fe_3O_4 while other authors showed that Ti-modified HA (TiHA) displays promising photocatalytic activity,[7,15,16] and good antibacterial properties.[17] Tsukada *et al.* [7] reported a band gap energy of 3.65 eV for a Ti^{4+} substituted HA with promising performances for the photochemical degradation of small organic molecules like acetaldehyde vapor under

UV-VIS radiation, and Wakamura *et al.* [16] showed that Ti-OH groups on the surface of TiHA can have a positive influence on electron injection, transport rate and short-circuit current density.

It is frequently reported that Ti^{4+} ions substitute for Ca^{2+} ions in the HA lattice, which results in a modification of its crystal structure [15-18] and phosphate anions can be substituted by titanate anions by annealing of Ti-modified HA at 700-850°C.[19]

In this work, we report a novel polypyrrole (PPy)/TiHA composite comprising concentric layers of conductive PPy and then the wide band gap semiconductor layer of TiHA NPs on wool yarns, where the TiHA NPs are deposited using a bio-inspired method. The resulting fiber-based structure is a potential building block for use in flexible optoelectronic, such as flexible UV detectors and fabric integrated photovoltaics.

HA was chosen as the semiconductor bulk-material because of the simplicity with which it can be nucleated on surfaces by a bio-inspired mineralization approach,[20] its functional versatility [8-10] and the well-established photoelectric properties of Ti-modified HAs.[7,15,16,17,18] Four sets of TiHAs, all of which displayed band gap values comparable those of wide band gap semiconductors [21-23], were obtained by wet synthesis by adjusting the concentration of the titanium dopant in the growth solution. The TiHA sample displaying optimal properties was then deposited on PPy –coated wool fibers under room temperature by a bio-inspired mineralization, where this ensured that the wool fibers retained their flexibility and softness. These conditions also avoid the growth of coarser TiHA grains that form a brittle coating on the fiber surface that seriously compromise the fiber flexibility and the mechanical stability of the coating. Our successful deposition of thin films of HA on PPy-coated natural fibers therefore delivers a fiber-based building block which can potentially be used to generate a new class of flexible, optoelectronic devices.

PPy was chosen as the conductive polymer since it is an established material which has been successfully printed onto Lycra/cotton fabrics to produce resistive fabric strain sensors capable of detecting the posture and gesture of human body.[24-25] The PPy layer was doped with anthraquinone disulfonic acid (ADA) to improve its electrical conductivity, and with pyroglutamic acid (PyE) to promote the nucleation of the TiHA during mineralization.

Oriented self-assembled crystal growth onto various substrates (e.g. Indium Tin Oxide glass, Si/SiO_2 wafers, ZnO thin film etc), including PPy [26] for DSC fabrication has been proven succesful.[27] However, to the best of our knowledge neither stoichiometric or doped HAs, nor other calcium phosphates were ever mineralized onto a PPy layer, nor on natural fibers, to obtain a fiber-shaped building block for optoelectronic devices.

Finally, using a comprehensive combination of Raman and FT-IR spectroscopy, X-ray diffraction, scanning and transmission electron microscopy we performed a detailed characterization of the different components and the fiber-shaped building block.

2. Experimental Details

2.1 Synthesis of Titanium-substituted Hydroxyapatite

Samples were synthesized by modifying of a previously reported method.[12] Briefly, 10 g of $Ca(OH)_2$ (purity > 95%, Sigma-Aldrich) were added to 100 mL of Millipore water and then stabilized at 50.0 °C under constant stirring at 400 rpm for 30 min. A solution obtained by mixing 8.87 g of H_3PO_4 (85 wt% Merck) with 30 mL of deionized water was added drop-wise into the $Ca(OH)_2$ suspension, together with 30 mL of a titanium isopropoxide (purity > 97% Alfa Aesar) solution in isopropyl alcohol (purity ≥ 99.7% Sigma-Aldrich). A titanium-free HA (HAp) was synthesized by simple addition of H_3PO_4 to the $Ca(OH)_2$ suspension.

TiHAs were synthesized using increasing amounts of the titanium precursor to reach the molar percentage of Ti atoms with respect to P of 8%, 17%, 25% and 50%. The obtained

TiHAs were named respectively TiHA8, TiHA17, TiHA25, and TiHA50. The molar ratio between Ca and P was set to 1.70 and kept constant for all of the experiments. Once the simultaneous drop-wise addition of phosphoric acid and titanium isopropoxide was performed, the solution was kept at 50 °C under constant stirring at 400 rpm for 3 hours and left still at room temperature overnight. Samples were repeatedly washed with water and then freeze-dried. Finally, the obtained powders were ground in a mortar and sieved using a 150 μm mesh filter.

2.2 Chemical Analysis

The chemical composition of bulk samples was determined by an induced coupled plasma spectrometer (ICP-OES), (Liberty 200, Varian, US) employing wavelengths of 422.673 nm (Ca), 334.941 nm (Ti), and 213.618 nm (P). An aliquot of samples for ICP-OES were dissolved in a diluted HNO_3 solution (~ 2 wt%) prior to analysis.

2.3 Powder X-ray Diffraction Analysis (XRD)

X-ray diffraction patterns were collected using a D8 Advance Diffractometer (Bruker, Karlsruhe, Germany) equipped with a Lynx-eye position sensitive detector using Cu Kα radiation (λ = 1.54178 Å) generated at 40 kV and 40 mA, operating in the 2θ range between 10° and 80° with a step size (2θ) of 0.02° and a counting time of 0.5 s. The same conditions were used to collect diffraction patterns on samples heated at 700°C for 6 hours. Complementary analysis was performed on raw powders using the Diamond Light Source synchrotron beam line I11 (HR-PXRD), where the X-ray diffraction patterns were recorded in the 2θ range between 5° and 70° using a monochromatic radiation (beam energy 15 keV, λ = 0.825969 Å) and a 0.001° step size.

The structural and microstructural analysis of the samples was performed using the FullProf suite software,[28] based on the Rietveld refinement method and Fourier analysis of the HR-PXRD patterns. A Thompson-Cox-Hastings pseudo-Voigt peak-shape profile was used for

100 the refinement. The microstructural analysis, including both microstrain and crystallite size,
101 was evaluated using the anisotropic Popa approach in the 6/m hexagonal system for the
102 hydroxyapatite structure (R_0 to R_3 refined for anisotropic size factors and E1 to E3 for
103 anisotropic microstrain factors).[29] The instrumental contribution to the profile was taken into
104 account by using a LaB_6 instrumental standard. The degree of sample crystallinity was
105 calculated according to Eqn (1):

106 $$Cristallinity[\%] = 100\ \frac{C}{A + C} \qquad Eqn(1)$$

107 where *C* and *A* are the sum of peak area and the area between the peaks and the background in
108 the diffraction pattern, respectively.[30]

109 *2.4 Transformed Fourier - Infrared analysis (FTIR) and Raman Spectroscopy.*

110 FTIR spectra of the synthesized titanium apatite were collected at room temperature by using
111 an FTIR Nicolet 380 Thermo Electron Corporation spectrometer working in the range of
112 wavenumbers between 4000 cm^{-1} and 400 cm^{-1} at a resolution of 2 cm^{-1}. A finely ground,
113 approximately 0.05% (w/w) mixture of the sample in KBr was pressed into a transparent disk
114 using a hydraulic press and applying a pressure in the MPa range. The Infra-red splitting
115 factor (IR-SF) was calculated by adding the measured intensities of the two $\nu4(PO_4)_3$
116 vibration bands at 565 and 605 cm^{-1} in the absorbance mode and dividing their sum by the
117 intensity of the valley between these absorption bands and the baseline, after a baseline
118 correction between 1200 and 250 cm^{-1}.[31]

119 TiHA NPs were studied after thermal transformation as described by XRD and Raman
120 spectroscopy. Each sample was placed on a potassium-bromide substrate producing minimal
121 background signal, and the potassium-bromide substrate containing the sample was placed on
122 top of a glass slide in order to fit on the Raman microscope stage for experimentation. The
123 settings used for testing were the following: 532 nm laser, 20-25 mW laser power, 2 seconds

acquisition time, 90 accumulations, 50x long working distance lens (spatial resolution ~ 1μm) and 1800T diffraction grating. Decomposition and non-linear curve fitting of the Raman signals were performed on fifteen spectra collected for each sample using Igor Pro 6.37 software.

2.5 Zeta potential and Size Measurements

ζ-potential distributions of dried powders suspended in HEPES buffer at pH=7.4 were measured by dynamic light scattering (DLS) with a Zetasizer Nano ZS (Malvern Ltd., Worcestershire, UK) and were quantified by laser Doppler velocimetry as electrophoretic mobility using disposable electrophoretic cell (DTS1061, Malvern Ltd., Worcestershire, UK). Ten runs of 30 s were performed for each measurement and four measurements were carried out for each sample.

Zeta average values were obtained by suspending the dried powders in a 0.1 wt% sodium citrate buffer at pH 6.0. Twenty runs of 30 s each were collected in each measurement and for each sample.

2.6 Scanning and Transmission Electron Microscopy

The fiber surface morphology was analyzed by a field emission scanning electron microscope (FE-SEM, Carl Zeiss Sigma NTS GmbH Oberkochen, Germany) working at an accelerating voltage in the 1.0 - 5.0 kV range. Fibers were mounted on aluminum stubs using carbon tape and were dried under an IR lamp for 15 minutes before analysis.

Sample analysis by transmission electron microscopy was performed at the University of York, JEOL Nanocentre using a JEOL JEM 2011 LaB6 TEM, operating at 200 kV. The microscope was equipped with a Gatan 794 digital camera and a Thermo Fisher NS7 energy dispersive X-ray spectroscopy (EDX) system. Samples were ground using a pestle and mortar, sieved at 150 μm, and drop-cast from a methanol suspension onto a holey carbon copper TEM grid.

149 *2.7 Thermogravimetric Analysis*

150 The carbonate content was evaluated on dried samples by thermogravimetric analysis (TGA)
151 using a Stanton STA 1500 (Stanton, London, UK) apparatus. About 10 mg of apatite was
152 weighed in a platinum crucible and heated from room temperature to 1100 °C under nitrogen
153 flow. The heating rate was 10 °C/min and alumina was used as reference standard. The CO_3^{2-}
154 content was evaluated according to the weight loss observed between 550 and 950 °C.[32]

155 *2.8 Specific Surface Area (SSA)*

156 Samples SSA were measured at liquid nitrogen temperature (-196 °C) using Brunauer-
157 Emmet-Teller (BET) mode with a CONTROL 750 (CE Instruments) apparatus. HA powders
158 were dried in air at 100°C for 30 minutes before the analysis.

159 *2.9 Determination of Band Gap Values (E_g)*

160 For band gap determination and subsequent analysis, a UV-Vis spectrophotometer with an
161 integrating sphere was used. The equipment was calibrated with a Spectralon standard
162 (Labsphere SRS-99-010). The reflectance spectra were measured and converted into an
163 adsorption coefficient using Kubelka-Munk equation while the E_g value was determined from
164 the Tauc plot obtained following the method reported by Sangiorgi *et al*.[33] Each measurement
165 was carried out three times averaging the recorded values.

166 *2.10 Wool and Polypyrrole coatings*

167 Wool yarns were obtained from a commercial stock with linear mass density of 68 tex.
168 Polypyrrole (PPy) coated conductive fiber composites were produced by *in situ* chemical
169 oxidative polymerization of pyrrole (purity > 98% Sigma-Aldrich) on the surface of wool
170 yarns. The polymerization reaction was carried out at room temperature. Different aliquots of
171 antraquinone-2-sulfonic acid sodium salt monohydrate (ADA, purity > 97% Sigma-Aldrich)
172 were added to the pyrrole solutions to enhance PPy conductivity. 0.2 g of pyrrole were

dissolved in 20 mL of MilliQ water together with 0.3 g of ADA to obtain a molar ratio ADA/pyrrole of 25 mol%. Wool yarns (0.2 g) were soaked in the obtained solution for 5 minutes at room temperature and were then immersed in a Fe(III) solution prepared by dissolving 1 g of $FeCl_3 \cdot 6H_2O$ (purity > 97% Sigma-Aldrich) in 20 mL of MilliQ water. These two steps were repeated three times. Subsequently, the fibers were rinsed with water, centrifuged, recovered and dried overnight at 40°C. Hereafter, these ADA-doped PPy coated wool fibers are referred to as WAP.

PPy doped with pyroglutamic acid (PyE, purity > 99%, Sigma-Aldrich) coated fibers, hereafter referred to as WEAPs, were obtained by adding both ADA and PyE to the pyrrole water solution and following the same steps as described for WAP. Different quantities of PyE, corresponding to the 5.0 mol% (WEAP5) and 10.0 mol% (WEAP10) with respect to the pyrrole, were used to assess the effects of higher amounts of PyE on the conductivity and the nucleation of TiHA 25 on WEAPs fibers.

2.11 Linear Resistivity

Linear resistivity of PPy-coated wool yarns was measured with metal contacts placed 1 cm apart on the yarns using an Escort170 Digital Multimeter. Data were calculated as the average of eight tests. Prior to testing, the PPy-coated yarns were conditioned at 20 °C and 65 % of relative humidity for 24 h.

2.12 Bio-inspired mineralization of conductive fibers

The procedure described below was followed for the mineralization of WAP and WEAPs fibers. 1 g of $Ca(OH)_2$ and 200 mg of conductive fibers were added to 10 mL of Millipore water. The solution was poured into a closed vessel under magnetic stirring and kept to 50°C for 3 days. After, the solution was poured in a beaker and kept under magnetic stirring while a solution obtained by dissolving 0.87 g of H_3PO_4 in 3 mL of Millipore water was added

dropwise simultaneously to a solution of titanium isopropoxide dissolved in isopropyl alcohol to reach a Ti/P molar ratio of 25%, corresponding to the amount of Ti introduced for the synthesis of TiHA25. The solution was then poured again in a closed vessel and placed into a shaking incubator set at 50°C and left under agitation for 7 days.

2.13 Deformability and stress tests

The flexibility and the mechanical properties of the mineralized wool yarns were evaluated by subjecting mineralized WEAP5 yarns to 10 stretching/release cycles;[34] secondly, the deformability of the semiconductor was assessed by knotting WAEP5 yarns before and after mineralization and comparing fibers morphologies by SEM as reported in the literature for other flexible electronic devices.[35,36]

Finally, to assess the endurance to dipping process of the mineral layer, mineralized WAEP5 yarns were immersed in ethanol at 40 °C for 15 minutes to simulate a dipping process before being analyzed by SEM to check the eventual removal of the mineral phase from the fibers surface.

3. Results

3.1 TiHA nanoparticles hydrodynamic diameter and ζ-potential

The hydrodynamic diameter size distributions of all the samples is reported in Fig. S1, while their average hydrodynamic diameters, expressed as zeta average, with the relative polydispersity indices (Pdi), and the ζ-potentials of TiHA NPs determined by DLS are reported in Table S1. The hydrodynamic diameters of TiHAs increase together with the titanium doping extent, with two step increases: the first moving from TiHA8 to TiHA17, and the second moving from TiHA25 to TiHA50. Differences in the recorded zeta average can be due to a different superficial composition as to the modifications of TiHAs NPs morphology at increasing titanium concentrations. Aggregation seems to play a major role only in the case

of TiHA50 NPs, whose hydrodynamic dimeter size distribution curve (Fig. S1) shows an enlargement towards larger particles and an higher polydispersity index with respect to those of the other samples (Table S1).

Finally, the ζ-potentials of titanium-modified NPs are more negative with respect to that of HAp, with TiHA8, TiHA25, and TiHA50 NPs having similar superficial net charges and TiHA17 NPs having a sensibly more negatively charged surface.

3.2 Band gap values of TiHA nanoparticles

The band gap energies (E_g) determined using reflectance method and the Tauc equation show values between 3.0 eV and 3.5 eV. These results are suitable for photocatalytic, photovoltaic applications and more in general for optoelectronic applications requiring wide band gap semiconductors. While the experimental bandgap energy of pure HA determined by Tsukada *et al.* is 6.0 eV, the addition of even small amounts of Ti as in the case of TiHA8 decreases the bandgap to 3.88±0.01 eV, which is a value much closer to that of anatase TiO_2 (3.27 eV).[7] E_g decreases even further for the other samples containing more Ti and equals 3.73±0.01 eV, 3.68±0.02 eV and 3.54±0.01 eV for TiHA17, TiHA25 and TiHA50 respectively. E_g of the mineral phase formed on biomineralized PPy doped fibers is the same as the value recorded for powder samples.

3.3 Crystal structure of TiHA nanoparticles after thermal treatment

The X-ray diffraction patterns (XRD) shown in Fig. 1 confirm the apatitic structure (JCPDS no. 09-432) of the synthesized powders, including those with high degrees of titanium substitution. The diffraction profiles feature exclusively the typical diffraction peaks of carbonated HA, which tend to become broader with the increase in titanium doping level. A background radiation gain, due to the occurrence of an amorphous phase not detectable by XRD, is observable going from pure HAp to TiHA50. This background noise increases with the increasing doping extent of titanium HAs.

The crystallinity index of the powders, together with their cell parameters and the IR-SFs are reported in Table 1. The former decreases as the titanium concentration increases and drop notably compared to TiHA17, while no systematic variation of the lattice parameters with titanium content is detectable by XRD analysis showing little variation and values very close to those of reference HAp for all of the TiHAs. More in detail, the *a* and *c*-axes of all the samples are in the range between 9.424 Å – 9.441 Å, and 6.884 Å – 6.894 Å respectively, while the cell volume shows a slight increase from 529.5 for HAp up to 531.7 for TiHA50.

The results of the microstructural analysis and the relative HR-PXRD patterns recorded using synchrotron radiation are reported in Table S2 and Fig. S2 respectively. The general crystallite domain is elongated in *c*-axis direction (approximately 60±4 nm) compared to the perpendicular *a/b*-axes (24±4 nm.). The strain is also higher in *c*-axis orientation. Taking into account both the crystallite size and the lattice strain, the apatite domain size is not modified by the introduction of even high amounts of titanium during the synthesis.

It is interesting to note that the R-Bragg and the R-structure factors for the Rietveld refinement of TiHA50 slightly improve if titanate (TiO_4^{4-}) substitutes up to 7% of phosphate (PO_4^{3-}) (3.73/4.80 compared to 3.76/4.87 for HA structure and 3.91/5.01 for 10% Ti^{4+} substitution of Ca^{2+}).

Four peaks potentially corresponding to a second crystalline phase are observed at the 2θ values of 15.63°, 20.82°, 22.74° and 24.93° on TiHA8 and TiHA50 especially. Their resolution is accurately illustrated by the enlarged view of the HR-PXRD spectra collected on the latter sample, reported in Fig. S3. Several structures are tested to identify this phase, among titanium oxide (anatase, rutile and brookite)[37,38], calcium phosphate compounds (β-TCP, brushite, monetite, octacalcium phosphate)[39-42], titanium phosphate ($TiPO_4$)[43] and calcium titanium phosphate compounds ($CaTi_4(PO_4)_6$).[44] This last structure matches the

experimental pattern but the low number of observed reflections and their low relative intensities do not allow a solid identification.

The phase compositions tabulated in Table 2 are obtained by using the Rietveld refinement of the XRD profiles of powders heated at 700°C for 6 hours as reference. Our data show that HAp remained as pure HA phase after the thermal treatment, while for TiHA8 conversion of HA to *b*-TCP started occurring with no anatase formation. On the contrary, for TiHA with higher doping extents, the formation of a crystalline anatase phase is linearly related to the titanium introduced during the synthesis ($R^2 = 0.9474$ by linear least squares). The formation of *b*-TCP instead is not linear and reaches its maximum for TiHA17 (23.3 wt%) for which a value much higher with respect to both TiHA8 and TiHA50 is recorded.

3.4 Infrared and Raman spectroscopy

IR spectra of HAp and TiHAs are shown in Fig. 2. The principal peaks of the spectra recorded on TiHAs are characteristic of apatite and correspond to the absorption band of H_2O (broad peak at 3400 cm^{-1} and sharper peak at 1640 cm^{-1}), HPO_4^{2-} (1050, 970, 600, and 570 cm^{-1}), and OH^- (3570 cm^{-1}). Differences among the spectra are evident when comparing the IR-SFs in Table 1 of the phosphate group absorbing in the spectral region between 650 and 550 cm^{-1} magnified in Fig. 2b. The value of the IR-SF decreases with respect to HAp when titanium is introduced, with the exception of TiHA17 for which a value close to that of HAp is recorded. Another sensible difference is relative to the intensity of the OH librational band (631 cm^{-1}), which is pronounced in the IR spectra of HAp and TiHA25, while it almost disappears for the other samples.

The absorption peaks at 1480, 1400, and 880 cm^{-1} correspond to CO_3^{2-} on PO_4^{3-} sites, suggesting that all the samples are slightly carbonated. Carbonation of HA commonly occurs unless measures are taken to specifically exclude CO_2/CO_3^{2-} from the synthesis. These results are coherent with TGA data reported forward in the text.

The Raman spectrum collected on HAp powder heated at 700°C is used as reference to evaluate the impact of increasing Ti content on the Raman spectra acquired on the thermally treated TiHAs and are presented in Fig. 3. Different spectral regions displaying characteristic signals of HA (945-980 cm^{-1}, Fig. 3a) and TiO_2 (80-250 cm^{-1} and 300-850 cm^{-1}), respectively, are magnified in Fig. 3b and 3c for each of the synthesized samples. The prominent band seen at ~963 cm^{-1} is ascribed to the v_1 PO_4 stretching mode of HA. Careful analysis of the v_1 band indicates a small asymmetry on the lower wavelength side, which is due to a signal occurring at ~955-957 cm^{-1}.This could be ascribed to the presence of small amounts of poorly crystalline carbonated apatite and/or amorphous calcium phosphate. The mean position and full width at half maximum of the principal HA band as determined from the peak decomposition is ~ 963.5±0.5 cm^{-1} and ~ 6±0.3 cm^{-1} respectively. These are typical values reported in the literature for the v_1 phosphate mode in HA.[45]

Five Raman bands that are not present in the spectrum of HAp can be clearly observed in the spectra of all the TiHAs in Fig. 3b and 3c. These bands are found at 145, 197, 399, 518 and 640 cm^{-1} in excellent agreement with the Raman bands typically reported for anatase.[46] The doubly degenerate mode at 145 cm^{-1} is the strongest band for the anatase phase and it is conveniently used to investigate the evolution of TiO_2 as a function of titanium ion substitution in the apatite lattice. The area of this absorption band determined by its systematic fitting performed for all the TiHAs increases exponentially with the increasing concentration of Ti (Fig. 3d), in accordance with the higher amount of TiO_2 already detected by the analysis of XRD profiles collected on thermally treated TiHAs.

3.5 Chemical composition and structure of TiHA nanoparticles

The bulk chemical compositions determined from ICP-OES analysis of the as-synthesized TiHAs are reported in Table 3, together with the carbonation extent evaluated by the thermogravimetric analysis (TGA) as the weight loss occurring between 550 °C and 950 °C.

320 The amounts of titanium detected and nominally introduced during the synthesis are in a good
321 agreement. The Ca/P molar ratio in all of the TiHAs is higher with respect to that of pure
322 HAp, the highest value being recorded for TiHA17. The Ca/P ratio displayed by this latter
323 sample is significantly higher respect to those displayed by the other TiHAs which instead
324 feature similar values.
325 The (Ti+Ca)/P molar ratio increases as expected with increasing concentrations of titanium,
326 but this relation is not linear, being the value of TiHA17 higher than that of TiHA25.
327 Interestingly, the Ca/(P+Ti) molar ratios detected for TiHA8 and TiHA17 are close to the
328 Ca/P value of HAp, while those of TiHA25 and TiHA50 are much smaller and deviate
329 significantly from it. At this regard, it is important to notice that carbonation occurred with
330 similar extent (CO_3^{2-} < 2 wt%) in all of the synthesis.
331 An increasing trend of the SSA values with increasing titanium concentrations is recorded,
332 but differences are only relevant when comparing TiHAs with a high amount (TiHA25 and
333 TiHA50) with those with a short amount of Ti (TiHA8 and TiHA17), for which the highest
334 and the lowest SSA values have been respectively determined (the lowest values being
335 determined for HAp). On the other hand, after thermal treatment at 700°C the SSA of all the
336 powders dropped to values around 20 ± 2 m^2/g. Such an evident decrease is a well-known
337 effect caused by the densification of HA accompanied by grain growth induced by the thermal
338 annealing.
339 TEM analysis of the samples reveals that Hap is composed of NPs having well defined rod-
340 like morphologies (Fig. 4a), with lengths typically in the 100 – 300 nm size range and widths
341 of about 20 – 50 nm in good agreement with the XRD and HR-PXRD analysis. On the
342 contrary, TiHAs NPs are observed as agglomerates of rounded, platelet-like morphologies
343 (Fig. 4b-e). All samples exhibit primary particle dimensions of 100 – 200 nm, regardless of
344 the amounts of titanium introduced during their synthesis. Very small crystallites (< 20nm)

are occasionally observed only on TiHAs at high Ti concentrations. At this regard, it is reported in the literature that the fast hydrolysis of titanium isopropoxide precursor generates amorphous TiO_2 nanorods,[47] that however are not observed on TiHAs.

Porosity is detected in all the samples, including the unmodified HAp NPs magnified together with TiHA50 NPs in Fig.5a and 5b respectively, with nanopores having typical dimensions of < 20 nm as observed in some but not all of the rods and platelets.

The collected selected area electron diffraction patterns (SAED) reported in the insets in Fig. 4a-e reveal the occurrence of crystalline HA as the main phase of all the samples, but unassigned spots/rings suggest the presence of a secondary phase which is tentatively assigned to the occurrence of calcium titanium phosphate as already reported by HR-PXRD.

3.6 Polypyrrole coating on wool yarns

SEM pictures of bare natural wool fibers, WAP and WAEP5 are depicted in Fig. S4a-d, together with a scheme representing a transversal section of wool yarns coated with a PPy layer doped with ADA and PyE (Fig. S4a, dopant molecules are not accurately positioned in the scheme). A change in surface morphology is observable starting from natural wool (Fig. S4b) to WAP fibers (Fig. S4c) that becomes rugged and features the occurrence of small round shaped particles of PPy. The surface roughness is further increased in WAEP (Fig. S4d) by the addition of 5 mol% of PyE, resulting in the formation of bigger round particles of PPy with a diameter around 1 μm. The resistivity of PPy coated fibers is found to be of a few kΩ / cm (Table S3), some units lower than those already reported in the literature for related PPy-coated synthetic fibers,[48] with a sensible increase of conductivity for the PPy doped with both ADA and PyE . No changes in the fiber surface morphology (picture not shown), nor further resistance reductions or increase in the mineralization extent (data reported below) could be observed with the increasing concentration of PyE from 5 up to 10 mol% of PPy for WAEPs fibers.

370 *3.7 Mineralization of PPy-conductive wool yarns with TiHA*

371 SEM pictures at increasing magnification of WAP, WAEP5 and WAEP10 fibers mineralized
372 with TiHA25 are presented in Fig. 6a-b, 6c-d and 6e-f respectively.

373 No differences in the TiHA25 coating extent nor in the nanoparticles morphology can be
374 observed from the SEM pictures collected on mineralized WAEP5 and WAEP10 reported in
375 Fig.6c-d and Fig.6e-f respectively, both presenting only a few bare areas on their surface
376 which is largely covered by a layer of NPs deposited during the mineralization process.

377 On the other hand, mineralization experiments carried out on WAP produce fibers poorly
378 coated with TiHA25 NPs with a similar surface morphology compared to that of
379 unmineralized fibers, and reported respectively in Fig. 6a and Fig. S4c.

380 Higher magnification SEM imaging shows the presence of rod-like NPs – with morphologies
381 and dimensions very close to those determined by TEM analysis on TiHAs samples –
382 covering only the surface of WAEPs fibers (Fig. 6d and 6f), while the PPy covering the WAP
383 fibers is still visible after the mineralization (Fig. 6b).

384 The bottom phase precipitated during the mineralization experiments was analyzed by XRD
385 (data not showed) and displays a diffraction profile identical to that collected on TiHA25 for
386 both WAP and WAEPs. To further assess the similarity between the TiHA25 synthesized and
387 that mineralized on WAEPs fibers, the semiconductor layer was manually separated by the
388 fibers to be ground, sieved and analyzed as already described for synthesized TiHAs. The data
389 collected on the resulting samples are in perfect agreement with those already described for
390 TiHA25 powder, and thus are not reported further in the text to avoid data redundancy.

391 SEM pictures of knotted bare and mineralized WAEP5 yarns subjected to 10
392 stretching/release cycles are depicted respectively in Fig.7a and 7b, together with a picture of
393 a WAEP5 fiber mineralized with TiHA25 after dipping in ethanol in Fig. 7c. No significant
394 difference was noticed by comparing the flexibility of unmineralized and mineralized

WAEP5 yarns, with the latter retaining both the semiconductor coating and WAEPs yarns original deformability.

Finally, the semiconductor coating was not altered by the dipping in ethanol and conserved the original extension and morphology of mineralized WAEP5 fibers.

4. Discussion

4.1 TiHA physicochemical characterization

During the synthesis of the TiHAs titanium ions replace phosphate groups instead of calcium in the HA lattice giving powders with suitable photo-electrical properties for application as wide band gap semiconductors in flexible electronics, *e.g.* like photoanodes in DSC cells. The obtained powders have higher SSAs (101-146 m^2/g) with respect to those typically reported for conventional DSC semiconductors (30-80 m^2/g), and considering that high-performance photoanodes require a large surface area for dye adsorption, these results show that calcium-phosphate based photoanodes can potentially take up significantly more dye molecules compared to conventional ones (*i.e.* ZnO and TiO_2). One of the key factors determining such high SSAs is the nanoporosity, as it can be observed by the TEM pictures reported in Fig. 5a,b due to the isopropanol used during the synthesis. The pores are then formed by the incorporation of the titanium precursor as part of the reaction mixture which is trapped inside the forming NPs and then removed due to evaporation.

The elemental composition of TiHAs shows that the doping ions are completely or partially incorporated into hydroxyapatite lattice during the synthesis, as a variation of the Ca/P molar ratio from that recorded on pure HAp is detected and moreover as the increase of Ti from 0 to 17 molar % relative to P is followed by a rapid increase of the Ca/P molar ratio, corresponding to a phosphorous depletion or at least to a calcium enrichment, while the (Ti+Ca)/P molar ratio increases up to values not compatible with the substitution of Ca with Ti ions in the apatite structure. On the other hand, the Ca/(P+Ti) molar ratios of TiHA8 and

TiHA17 are close to the Ca/P ratio of reference HAp, suggesting more phosphorus than calcium replacement by titanium ions in the apatite structure.

This result is reinforced by the XRD analyses performed on thermally treated powders showing an increased crystallinity of the HA phase and the formation of β–TCP - which occurred for all the powders with the exception of HAp - due to the instability of the titanium-modified apatitic phase. In this regard, Raynaud *et al.* showed that HA with a Ca/P ratio lower than that of stoichiometric HA (1.67) start to decompose into *β*-TCP when heated in air at 700°C.[49] Thus, the thermal decomposition of TiHAs into triphasic mixtures of HA, β-TCP, and anatase is consistent with a deviation from the Ca/P molar ratio compared to that of HAp (for which no β-TCP was observed) due to the successful introduction of titanium in the apatite lattice. However, the data reported in the present study are only in partial agreement with what reported by Raynaud, as the formation of *β*-TCP from the TiHAs synthesized in this study appears to be related to a phosphorus rather than a calcium deficiency of the TiHA.

Anatase is absent in thermally treated HAp and TiHA8 and is produced only in small amounts during the thermal treatment of sample TiHA17, while large amounts of this phase are formed during the thermal decomposition of TiHA25 and TiHA50. The presence of perovskite ($CaTiO_3$), which was previously reported to be formed under calcination of titanium HAs,[50] is excluded instead for all the samples, but signals ascribable to an additional phase, probably $CaTi_4(PO_4)_6$, were detected from the HR-PXRD analysis of TiHA8 and especially of TiHA50. However, the identity of this phase could not be unambiguously assigned due to the low S/N ratio and the low number of peaks.

Also the TEM and the SAED analyses reveal the occasional presence of a secondary phase consisting of round shaped aggregated of very small crystallites (< 20 nm), especially in the cases of TiHA25 and TiHA50 NPs for which only partial substitution by titanium ions has occurred. The presence of such a secondary phase, which is likely to be amorphous TiO_2,

could be one of the factors determining the slightly larger surface areas of TiHA25 and TiHA50 with respect to TiHA8 and TiHA17.

It is worth noting that the titanium precursor used during the synthesis is a titanium alkoxide with small alkyl chains and that both these features comply with a fast hydrolysis kinetic due to the easiness with which the Ti coordination sites occupied by alkyl chains are hydrolyzed.[51] Sol-gel synthesis of TiO_2 by fast hydrolysis of titanium alkoxide precursor carried out at low temperature give amorphous titanium dioxide NPs,[52] that upon thermal treatment can be converted into crystalline anatase [53] corroborating the hypothesis of amorphous TiO_2 formation during the synthesis of TiHA.

The occurrence of amorphous TiO_2 only for Ti concentration values above 17 molar % with respect to P can be explained by the preferential substitution of PO_4^{3-} with oxy/hydroxy anions of Ti (*i.e.* ions with a general formula $H_xTiO_y^{4+x-2y}$) up to this Ti/P molar ratio - that is to say, up to a value of 10% for the Ti/Ca ratio. Above this concentration the excess of titanium precursor is oxidized to amorphous TiO_2. Such mechanism is in partial agreement with what reported by Tsukada *et al*. who described the formation of particles of amorphous titanium phosphate through the synthesis of titanium-modified HA, when the titanium concentration Ti/(Ca+Ti) exceeded 10%, hypothesizing the one-to-one substitution of Ca^{2+} with Ti^{4+}.[7]

The data presented in this work provides strong evidence that Ti^{4+} ions replace PO_4^{3-}, but even if the decrease of the Bragg factor relative to the Rietveld refinement of the HR-PXRD pattern of TiHA50 suggests the substitution of phosphate by titanate ions, similarly to what is already described on sintered TiHAs in the litterature,[54] it was not possible to assure whether phosphates is substituted by titanate, titanium oxy/hydroxide, or other titanium anions in the apatitic lattice.

On the other hand, the replacement of PO_4^{3-} instead of Ca^{2+} by titanium doping is in contrast to the theoretical calculation for Ti-substituted HA reported by Yin *et al.* using density functional theory, where only the occurrence of $[Ti(OH)_x]^{4-x}$ ions - with x ranging from 0 to 2 - was considered in place of calcium, excluding phosphates from the calculations.[54] Ti^{4+} has a smaller atomic radius and a higher valence respect to Ca^{2+} (0.074 nm and 0.110 nm respectively for 6-coordinate Ti^{+4} and 6-coordinate Ca^{2+} respectively), thus their direct interchange seems unlikely unless the titanium precursor introduced during the synthesis oxidizes to generate $[Ti(OH)_x]^{4-x}$ ions with a larger molecular radius and a charge similar to that of Ca^{2+}. However, several studies reported assert that the direct substitution of Ca^{2+} with Ti^{4+} is a possible pathway. [15,16,54,55,56] For instance, Anmin *et al.* [55] attributes the decrease of HAp cell volume to a direct Ca^{2+} replacement with Ti^{4+}, while other studies suggest that titanium can replace calcium only as a divalent ionic group, that is to say as $[Ti(OH)_2]^{2+}$ and/or $[Ti(HPO_4)]^{2+}$.[15,16] This substitution mechanism is also supported by two further publications, one on the manufacturing of TiHA by ionic exchange through a dissolution/precipitation mechanism in the presence of a divalent titanium precursor,[56] and the other on the computational calculations carried out on TiHA which reports a strong preference for $Ti(OH)_2^{2+}$ occupancy on Ca(2) site up to a Ti/Ca 10 % ratio.[54]

Nevertheless, in this work we report that titanium actually replaces phosphorous up to Ti/P 17 molar %, while above this concentration a secondary phase probably consisting of round aggregates of small crystallites of amorphous TiO_2 starts to occur. This phase is not identifiable by XRD analysis but could be occasionally detected by TEM as NPs in TiHA25 and TiHA50, and indirectly as anatase from the XRD profiles and from the Raman spectra of thermally treated powders.

Regardless of the amount of doping ions introduced during the synthesis, the band gap value of HA is sensibly moved towards a suitable band gap range for application in photoactive

devices by titanium doping. The recorded values are in perfect agreement with those reported by Tsukada *et al*.,[7] despite the fact that, as already mentioned, he attributes the introduction of Ti into the HA lattice to Ca instead of P substitution.

As a result of the optimized band gap energy, SSA and microstructure compared to the samples with lower Ti content we selected sample TiHA25 for mineralization experiments on WAP and WEAPs yarns. TiHA25 was also preferred to TiHA50 for the better dispersion of its NPs in water suspension, as evidenced by the lower Z-average value and its hydrodynamic diameter distribution, all being important factors for the mineralization process affecting the homogeneity of fiber surface coating.

4.2 Bio-inspired mineralization of TiHA on polypyrrole coated wool fibers

The successful nucleation of TiHA25 on PPy-coated conductive wool fibers provides a proof of concept for the assembly of fabric integrated electronic devices through two simple processes like oxidative polymerization of PPy and TiHA controlled bio-inspired mineralization. A pivotal role in the deposition of TiHA on the conductive wool yarns is played by the doping of the PPy coating with PyE that modifies the physicochemical properties of the PPy layer by increasing its wettability, and promotes the nucleation of TiHA25 on its surface by means of its carboxyl group.

Without PyE molecules, PPy-coated wool fibers are much more hydrophobic and more importantly TiHA25 could not be mineralized on their surfaces. In this regard, it is worthy to note that PyE was chosen as dopant not only because of its similarity to the pyrrole molecules – as can be seen from the scheme in Fig. S4a – but also because it displays a carboxylic moiety.

In this respect, Toworfe G.K. *et al*.[57] demonstrated that carboxylic modified surfaces are more hydrophilic than those modified with amines and hydroxyls, in accordance with the increased wettability of the PPy-coated fibers observed during the mineralization of TiHA25. Moreover,

519 compounds containing the carboxyl or amine functional group are largely reported to foster
520 the adsorption and crystallization of calcium phosphates,[58-60] as in the case of collagen
521 molecules, whose carboxylate moieties are supposed to be responsible for the nucleation of
522 HA NPs on collagen from SBF solution.[61,62]
523 The introduction of PyE in PPy considerably increases TiHA25 deposition on the PPy-coated
524 wool fibers, and surprisingly its introduction prompts an increase of conductivity of the PPy
525 layer. No differences are observable by doubling the amount of PyE, *i.e.* passing from a
526 PyE/pyrrole ratio of 5 mol% to a 10 mol%, for both the increased TiHA NPs mineralization
527 and PPy raise of conductivity. On the other hand, the combination of ADA and PyE results in
528 a further increase of conductivity, but whether this additional conductivity raise is due to the
529 intrinsic property of PyE or to the augmented quantities of PPy deposited on the fiber surface
530 cannot be unambiguously decided, as the introduction of PyE is likely to cause both the
531 effects. Also, the PPy conductivity is largely affected by the increased overall layer
532 thickness.[63]
533 As we have shown, the electrical resistivity of the PyE-doped PPy layers is promising for
534 functional and flexible electronic devices. There is evidence provided by J. Wu *et al.* [64] who
535 report significantly better values for conductive layers made of this organic polymer,
536 demonstrating that a further improvement of its conductivity performance can be achieved in
537 the future. Our studies show that PyE prompts the nucleation of rod-like TiHA nanocrystals
538 retaining the chemical composition, morphology, SSA and band gap values of the parental
539 TiHA powders, proving the applicability of bio-inspired approach for the obtainment of fiber-
540 shaped optoelectronic flexible devices. On the contrary, WAP fibers were not successfully
541 covered by TiHA25 during the mineralization process, with only a small deposition of
542 mineral phase on some areas of its surface.

543 The nanometric size of the semiconductor layer is probably the principal factor determining
544 the retention of WAEPs yarns deformability after TiHA25 mineralization that would be lost
545 in case of the deposition of coarser grains as induced by the thermal treatment of TiHAs.
546 Thus, even if it is well known that the physicochemical and properties of HA can be
547 optimized by thermal annealing, this will also determine the formation of a brittle
548 ceramic layer limiting the flexibility of the fiber and eventually facilitating its peeling-off
549 from the conductive PPy layer. Moreover, the high SSA displayed by TiHAs
550 semiconductor layer would be impaired by the thermal treatment determining its
551 remarkable reduction up to the 85% of the original. A large SSA is in fact a highly
552 desirable feature in wide band gap semiconductors that could be exploited *e.g*. by
553 adsorbing dye molecules onto them to increase their photoelectric performances. An
554 easy way to achieve the incorporation of dyes in semiconductors is by dipping them into
555 an organic solvent. At this regard, the TiHA layer mineralized on the surface of WAEP5
556 fibers endured to a simulated dipping process into ethanol at 40°C, preserving its
557 extension and adhesion on the PPy layer.
558 To the best of our knowledge, no work reporting the mineralization of HA, nor of other
559 calcium phosphates on PPy is present in the literature, even though numerous works report
560 the coating of this highly conductive polymer using TiO_2,[65] ZnO,[21] other metallic oxides and
561 materials like carbon nanotubes.[22,23,65]
562 One of the key challenges in the future is the retention of fiber flexibility after semiconductor
563 deposition. For this purpose we aim to develop a procedure using a protective layer, or by an
564 electrolyte and a redox mediator in the case of a flexible fiber-shaped DSCs device.[66]

565

566 **5. Summary and Conclusions**

Four hydroxyapatite based samples modified with increasing amounts of titanium were successfully obtained and their suitability to work as semiconductors in flexible electronic devices was evaluated by measuring their physico-chemical properties, paying particular attention to their band gap values and their SSAs.

During their precipitation, titanium was found to replace phosphorous in the apatite lattice up to Ti/P 17% molar ratio, with the occasional formation of negligible amounts of $CaTi_4(PO_4)_6$, while the excess of doping ions was rapidly oxidized to amorphous titanium dioxide.

Optimized properties were identified for a 25 molar% of Ti/P, corresponding to a Ti/Ca content of 15 molar%. This material was deposited onto the surface of conductive wool yarns produced by *in situ* chemical oxidative polymerization of pyrrole directly on the fibers surface. This step was made possible by the doping of the resulting polypyrrole layer with antraquinone-2-sulfonic acid, used to enhance the electric conductivity, and pyroglutamic acid which rendered more hydrophilic the conductive layer and, thanks to its carboxylic moiety, drove the nucleation of apatite on the polypyrrole surface.

In conclusion, this work reports the successful production through simple processes like oxidative polymerization and mineralization, of a concentric fiber-shaped building block designed for flexible optoelectronic devices and consisting of a layer of titanium-modified HA (wide band gap semiconductor) nucleated on a layer of polypyrrole (conductive layer) supported by wool natural fibers, that may find useful applications in radiation sensors, photocatalytic devices and wearable electronics.

Acknowledgements

This work was supported by the European Union 7th Framework Program under the Grant Agreement n°310637 SMILEY. We thank Diamond Light Source for access to the High Resolution Powder Diffraction beamline I11. Pierre GRAS would like to thank INP Toulouse

592 for the financial support of his 1 month secondment in Italy. This research is supported by the
593 ANR “Agence Nationale de la Recherche” (ref: Innov’Hap: ANR-12-BS09-0030) and
594 “Region Midi-Pyrenées” (CLE n°12052853).

References

[1] M. Caironi; T.D. Anthopoulos, Y.Y. Noh, J. Zaumseil, Organic and hybrid materials for flexible electronics. *Adv Mat*. 2013, **25**, 4208-4209.

[2] S Akhtar, M.S. Alghamdi, Y.G. Malik, M.A. Khalil, R.M.A. Riaz, S. Naseem, Structural, optical, magnetic and half-metallic studies of cobalt doped ZnS thin films deposited via chemical bath deposition. *J. Mater. Chem. C*, 2015, **3**(26), 6755-6763.

[3] M.Y Yen, M.C. Hsiao, S.H. Liao, P.I Liu, H.M Tsai, C.C.M. Ma, N.W. Pu, M.D. Ger, Preparation of graphene/multi-walled carbon nanotube hybrid and its use as photoanodes of dye-sensitized solar cells. *Carbon.*, 2011, **49,** 3597-3606.

[4] J. Zhang, W. Peng, Z. Chen, H. Chen, L. Han, Effect of cerium doping in the TiO2 photoanode on the electron transport of dye-sensitized solar cells. *J. Phys. Chem. C*, 2012, **116,** 19182-19190.

[5] Y. Duan, N. Fu, Q. Liu, Y. Fang, X. Zhou, J. Zhang, Y. Lin, Sn-doped TiO2 photoanode for dye-sensitized solar cells. *J. Phys. Chem. C*, 2012, **116**, 8888-8893.

[6] A. Latini, C. Cavallo, F.K. Aldibaja, D. Gozzi, D. Carta, A. Corrias, L. Lazzarini, G. Salviati, Efficiency improvement of DSSC photoanode by scandium doping of mesoporous titania beads. *J. Phys. Chem. C*, 2013, **117**, 25276-25289.

[7] M. Tsukada, M. Wakamura, N. Yoshida, T. Watanabe, Band gap and photocatalytic properties of Ti-substituted hydroxyapatite: Comparison with anatase-TiO_2. *J. Mol. Catal. A-Chem.*, 2011, **338,** 18-23.

[8] X. Wang, Y Sun, K. Lin, Facile synthesis of dental enamel-like hydroxyapatite nanorod arrays via hydrothermal transformation of hillebrandite nanobelts. *J. Mater. Chem. B*, 2015, **3**(37), 7334-7339.

[9] Z. Wei, C. Xu, B. Li, Application of waste eggshell as low-cost solid catalyst for biodiesel production. *Bioresource Technol.*, 2009, **100**, 2883-2885.

[10] M. Uota, H. Arakawa, N. Kitamura, T. Yoshimura, J. Tanaka, T. Kijima, Synthesis of high surface area hydroxyapatite nanoparticles by mixed surfactant-mediated approach. *Langmuir*, 2005, **21,** 4724-4728.

[11] Y.P. Guo, T. Long, S. Tang, Y.J. Guo, Z.A. Zhu. Hydrothermal fabrication of magnetic mesoporous carbonated hydroxyapatite microspheres: biocompatibility, osteoinductivity, drug delivery property and bactericidal property. *J. Mater. Chem. B*, 2014, **2**(19), 2899-2909.

[12] M. Iafisco, C. Drouet, A. Adamiano, P. Pascaud, M. Montesi, S. Panseri, S. Stephanie, A. Tampieri, Superparamagnetic iron-doped nanocrystalline apatite as a delivery system for doxorubicin. *J. Mater. Chem. B*, 2016, **4**(1), 57-70.

[13] V. Iannotti, A. Adamiano, G. Ausanio, L. Lanotte, G. Aquilanti, J.M.D. Coey, M. Lantieri, G. Spina, M. Fittipaldi, G. Margaris, K. Trohidou, S. Sprio, M. Montesi, S. Panseri, M. Sandri, M. Iafisco, A. Tampieri. Fe-Doping-Induced Magnetism in Nano-Hydroxyapatites. *Inorg. Chem.,* 2017, **56**(8)*,* 4446–4458.

[14] Y. Liu, H. Zhong, L. Li, C. Zhang, Temperature dependence of magnetic property and photocatalytic activity of Fe 3 O 4/hydroxyapatite nanoparticles. *Mater. Res. Bull.*, 2010, **45**, 2036-2039.

[15] M. Nishikawa, W. Yang, Y. Nosaka, Grafting effects of Cu 2+ on the photocatalytic activity of titanium-substituted hydroxyapatite. *J of Mol Catal A-Chem.*, 2013, **378**, 314-318.

[16] M. Wakamura, K. Hashimoto, T. Watanabe, Photocatalysis by calcium hydroxyapatite modified with Ti (IV): albumin decomposition and bactericidal effect. *Langmuir*, 2003, **19**, 3428-3431.
[17] K. Kandori, T. Kuroda, M. Wakamura, Protein adsorption behaviors onto photocatalytic Ti(IV)-doped calcium hydroxyapatite particles, *Colloids Surf. B.*, 2011, **87**, 472–479.
[18] C.C. Ribeiro, M.A. Barbosa, A.A.S.C. Machado, A. Tudor, M.C. Davies, Modifications in the molecular structure of hydroxyapatite induced by titanium ions. *J. Mater. Sci-Mater. M.*, 1995, **6**, 829-834.
[19] A. Ślósarczyk, A. Zima , Z. Paszkiewicz , J. Szczepaniak , A.H. De Aza , A. Chróścicka, The influence of titanium on physicochemical properties of Ti-modified hydroxyapatite materials. Materiały Ceramiczne /Ceramic Materials/, 2010, **62**(3), 369-375
[20] Z. Wang, Z. Xu, W. Zhao, N. Sahai. A potential mechanism for amino acid-controlled crystal growth of hydroxyapatite. *J. Mater. Chem. B*, 2015, **3**(47), 9157-9167.
[21] C.A. Ferreira, S.C. Domenech, P.C. Lacaze, Synthesis and characterization of polypyrrole/TiO2 composites on mild steel. *J. Appl. Electrochem.*, 2001, **31**, 49-56.
[22] Y. Hao, M. Yang, W. Li, X. Qiao, L. Zhang, S. Cai, A photoelectrochemical solar cell based on ZnO/dye/polypyrrole film electrode as photoanode. *Sol. Energ.Mat. Sol. C.*, 2000, **60**, 349-359.
[23] J. Zhang, S. Wang, M. Xu, Y. Wang, H. Xia, S. Zhang, X. Gou, S. Wu, Polypyrrole-coated SnO2 hollow spheres and their application for ammonia sensor. *J. Phys. Chem. C.*, 2009, **113**, 1662-1665.
[24] E.P. Scilingo, F. Lorussi, A. Mazzoldi, D. De Rossi, Strain-sensing fabrics for wearable kinaesthetic-like systems. *IEEE Sens. J.*, 2003, **3**, 460.
[25] F. Lorussi, W. Rocchia, E.P. Scilingo, A. Tognetti, D. De Rossi, Wearable, redundant fabric-based sensor arrays for reconstruction of body segment posture. *IEEE Sens. J.*, 2004, **4**, 807.
[26] Y. Li, G. Shi. Electrochemical growth of two-dimensional gold nanostructures on a thin polypyrrole film modified ITO electrode. *J. Phys. Chem. B.*, 2005, **109,** 23787-23793.
[27] L. Vayssieres, Growth of arrayed nanorods and nanowires of ZnO from aqueous solutions. *Adv. Mat.*, 2003, **15**, 464-466.
[28] J. Rodríguez-Carvajal, Recent Developments of the Program FULLPROF, Commission on Powder Diffraction (IUCr) Newsletter, 2001, 26, 12-19.
[29] N. Sangiorgi, L. Aversa, R. Tatti, R. Verucchi, A. Sanson, Spectrophotometric method for optical band gap and electronic transitions determination of semiconductor materials. *Opt. Mater.,* 2017, **64**, 18-25.
[30] N.C. Popa, The (hkl) Dependence of Diffraction-Line Broadening Caused by Strain and Size for All Laue Groups in Rietveld Refinement. *J. Appl. Cryst.*, 1998, **31**, 176-180
[31] M. Iafisco, B. Palazzo, G. Martra, N. Margiotta, S. Piccinonna, G. Natile, V. Gandin, C. Marzano, N. Roveri, Nanocrystalline carbonate-apatites: role of Ca/P ratio on the upload and release of anticancer platinum bisphosphonates. *Nanoscale*, 2012, **4**, 206-217.
[32] A. Adamiano, D. Fabbri, G. Falini, M.G. Belcastro, A complementary approach using analytical pyrolysis to evaluate collagen degradation and mineral fossilisation in archaeological bones: The case study of Vicenne-Campochiaro necropolis (Italy). *J. Anal. App. Pyrol.*, 2013, **100**, 173-180.

[33] M. Iafisco, E. Varoni, E. Battistella, S. Pietronave, M. Prat, N. Roveri, L. Rimondini, The cooperative effect of size and crystallinity degree on the resorption of biomimetic hydroxyapatite for soft tissue augmentation. *Int. J. Artif. Organs.*, 2010, **33**, 765–774.
[34]. X. Huang, Z. Yu, S. Huang, Q. Zhang, D. Li, Y. Luo, Q. Meng, Preparation of fluorine-doped tin oxide (SnO2:F) film on polyethylene terephthalate (PET) substrate, *Mater. Lett.*, 2010, **64**, 1701–1703.
[35] R. Xu, J. Wei, F. Guo, X. Cui, T. Zhang, H. Zhu, K. Wang, D. Wu. Highly conductive, twistable and bendable polypyrrole–carbon nanotube fiber for efficient supercapacitor electrodes. *RSC Adv.*, 2015, ***5***(28), 22015-22021.
[36] R. Cruz-Silva, A. Morelos-Gomez, H.I. Kim, H.K. Jang, F. Tristan, S. Vega-Diaz, L.P. Rajukumar, A.L. Elías, N. Perea-Lopez, J. Suhr, M. Endo. Super-stretchable graphene oxide macroscopic fibers with outstanding knotability fabricated by dry film scrolling. *ACS nano*, 2014, ***8***(6), 5959-5967.
[37] C. J. Howard, T. M. Sabine, F. Dickson, Structural and thermal parameters for rutile and anatase, *Acta Cryst.*, 1991, **B47**, 462-468.
[38] E. P. Meagher, G. A. Lager, Polyhedral thermal expansion in the TiO_2 polymorphs: refinement of the crystal structures of rutile and brookite at high temperature, *The Canadian Mineralogist*, 1979, **17**, 77-85.
[39] M. Yashima, A. Sakai, T. Kamiyama, A. Hoshikawa, Crystal structure analysis of β-tricalcium phosphate $Ca_3(PO_4)_2$ by neutron powder diffraction, *J. Solid State Chem.*, 2003, **175**(2), 272-277.
[40] P. F. Schofield, K.S. Knight K S, J. A. M. van der Houwen, E. Valsami-Jones, The role of hydrogen bonding in the thermal expansion and dehydration of brushite, di-calcium phosphate dehydrate, *Phys. Chem. Miner.*, 2004, **31**, 606-624.
[41] M. Catti, G. Ferraris, A. Filhol, Hydrogen bonding in the crystalline state. CaHPO4 (monetite), P-1 or P1? A novel neutron diffraction study, *Acta Crystallogr.*, 1997, **B33**, 1223-1229.
[42] W.E. Brown, Octacalcium phosphate and hydroxyapatite: crystal structure of octacalcium phosphate, *Nature,* 1962. **196,** 1048 – 1050.
[43] A. Leclaire, A. Benmoussa, M. M. Borel, A. Grandin, B. Raveau, $TiPO_4$, a titanium orthophosphate with a $CrVO_4$ sublattice, *Eur. J. Solid State Inorg. Chem.*, 1991, **28**, 1323-1333.
[44] P. Villars, Material Phases Data System (MPDS), CH-6354 Vitznau, Switzerland (ed.) Springer Materials Ca0.5Ti2(PO4)3 (CaTi4[PO4]6) Crystal Structure, http://materials.springer.com/isp/crystallographic/docs/sd_1621200.
[45] G. Penel, G. Leroy, C. Rey, E. Bres, MicroRaman spectral study of the PO4 and CO3 vibrational modes in synthetic and biological apatites. *Calcif. Tissue Int.*, 1998, **63**(6), 475-481.
[46] H.C. Choi, Y.M. Jung, S.B. Kim, Size effects in the Raman spectra of TiO_2 nanoparticles. *Vib. Spectrosc.*, 2005, **37**(1), 33-38.
[47] P.D. Cozzoli, A. Kornowski, H. Weller, Low-temperature synthesis of soluble and processable organic-capped anatase TiO2 nanorods. *J. Am. Chem. Soc.*, 2003, **125**, 14539-14548.

[48] Y. Li, X.Y. Cheng, M.Y. Leung, J. Tsang, X.M. Tao, M.C.W. Yuen, A flexible strain sensor from polypyrrole-coated fabrics. *Synthetic Met.*, 2005, **155**, 89-94.
[49] S. Raynaud, E. Champion, D. Bernache-Assollant, Calcium phosphate apatites with variable Ca/P atomic ratio II. Calcination and sintering. *Biomaterials*, 2002, **23**, 1073-1080.
[50] C. Paluszkiewicz, J. Czechowska, A. Ślósarczyk, Z. Paszkiewicz, Evaluation of a setting reaction pathway in the novel composite TiHA–CSD bone cement by FT-Raman and FT-IR spectroscopy. *J. Mol. Struct.*, 2013, **1034**, 289-295.
[51] D.D. Dunuwila, C.D. Gagliardi, K.A. Berglund, Application of controlled hydrolysis of titanium (IV) isopropoxide to produce sol-gel-derived thin films. *Chem. Mater.*, 1994, **6**, 1556-1562.
[52] Z. Zhao, B.K. Tay, G. Yu. Room-temperature deposition of amorphous titanium dioxide thin film with high refractive index by a filtered cathodic vacuum arc technique. *Appl. Optics*, 2004, **43**, 1281-1285.
[53] H. Zhang, M. Finnegan, J.F. Banfield, Preparing single-phase nanocrystalline anatase from amorphous titania with particle sizes tailored by temperature. *Nano Lett.*, 2001, **1**, 81-85.
[54] S. Yin, D.E. Ellis. First-principles investigations of Ti-substituted hydroxyapatite electronic structure. *Phys. Chem. Chem. Phys.*, 2010, **12**, 156-163.
[55] H. Anmin, L. Ming, C. Chengkang, M. Dali. Preparation and characterization of a titanium-substituted hydroxyapatite photocatalyst. *J. Mol. Catal. A-Chem.*, 2007, **267**, 79
[56] C.C. Ribeiro, I. Gibson, M.A. Barbosa. The uptake of titanium ions by hydroxyapatite particles – structural changes and possible mechanisms. *Biomaterials*, 2006, **27**, 1749-1761.
[57] G.K. Toworfe, R.J. Composto, I.M. Shapiro, P. Ducheyne. Nucleation and growth of calcium phosphate on amine-, carboxyl-and hydroxyl-silane self-assembled monolayers. *Biomaterials*, 2006, **27**, 631-642.
[58] N. Spanos, P.G. Klepetsanis, P.G. Koutsoukos. Model studies on the interaction of amino acids with biominerals: the effect of L-serine at the hydroxyapatite–water interface. *J. Colloid Interf. Sci*., 2001, **236**, 260-265.
[59] W. Li, Y. Cai, Q. Zhong, Y. Yang, S.C. Kundu, J. Yao, Silk sericin microcapsules with hydroxyapatite shells: protection and modification of organic microcapsules by biomimetic mineralization. *J. Mater. Chem. B*, 2016, **4**(2), 340-347.
[60] M. Tanahashi, T. Matsuda, Surface functional group dependence on apatite formation on self-assembled monolayers in a simulated body fluid. *J. Biomed. Mater. Res.*, 1997, **34**, 305-315.
[61] R. Shahlori, G.I. Waterhouse, A.R. Nelson, D.J. Mc Gillivray, Morphological, chemical and kinetic characterisation of zein protein-induced biomimetic calcium phosphate films. *J. Mater. Chem. B*, 2015, **3**(30), 6213-6223.
[62] S.H. Rhee, J.D. Lee, J. Tanaka, Nucleation of hydroxyapatite crystal through chemical interaction with collagen. *J. Am. Chem. Soc.*, 2000, **83**, 2890-2892.
[63] A.C. Fou, M.F. Rubner, Molecular-level processing of conjugated polymers. 2. Layer-by-layer manipulation of in-situ polymerized p-type doped conducting polymers. *Macromolecules*, 1995, **28**, 7115-7120.
[64] J. Wu, Q. Li, L. Fan, Z. Lan, P. Li, J. Lin, S. Hao. High-performance polypyrrole nanoparticles counter electrode for dye-sensitized solar cells. *J. Power Sources*, 2008, **181**, 172-176.
[65] Y. Wang, W. Jia, T. Strout, A. Schempf, H. Zhang, B. Li, J. Cui, Y. Lei, Ammonia gas sensor using polypyrrole-coated TiO_2/ZnO Nanofibers. *Electroanal.*, 2009, **21**, 1432-1438.

[66] S. Sahoo, G. Karthikeyan, G.C. Nayak, C.K. Das, Electrochemical characterization of in situ polypyrrole coated graphene nanocomposites. *Synthetic Met.*, 2011, **161**, 1713-1719.

Statement Contribution of Authors

Conception of the work:
Alessio Adamiano, Anna Tampieri, Alessandra Sanson

Design of the work:
Alessio Adamiano, Andrea Ruffini

Data collection:
Alessio Adamiano, Nicola Sangiorgi, Konstantinos Chatzipanagis, Matthew Bilton, Bartosz Marzec, Alessio Varesano.

Data analysis and interpretation:
Alessio Adamiano, Nicola Sangiorgi, Pierre Gras, Konstantinos Chatzipanagis, Alessio Varesano, Roland Kröger

Drafting the article:
Alessio Adamiano

Critical revision of the article:
Simone Sprio, Monica Sandri, Alessandra Sanson, David Grossin, Christine Francès, Fiona Meldrum, Roland Kroeger, Anna Tampieri

Final approval of the version to be published:
Alessio Adamiano, Nicola Sangiorgi, Simone Sprio, Andrea Ruffini, Monica Sandri, Alessandra Sanson, Pierre Gras, David Grossin, Christine Francès, Konstantinos Chatzipanagis, Matthew Bilton, Bartosz Marzec, Alessio Varesano, Fiona Meldrum, Roland Kröger, Anna Tampieri.

Conflict of interest

There are no conflicts of interest to declare

Figures

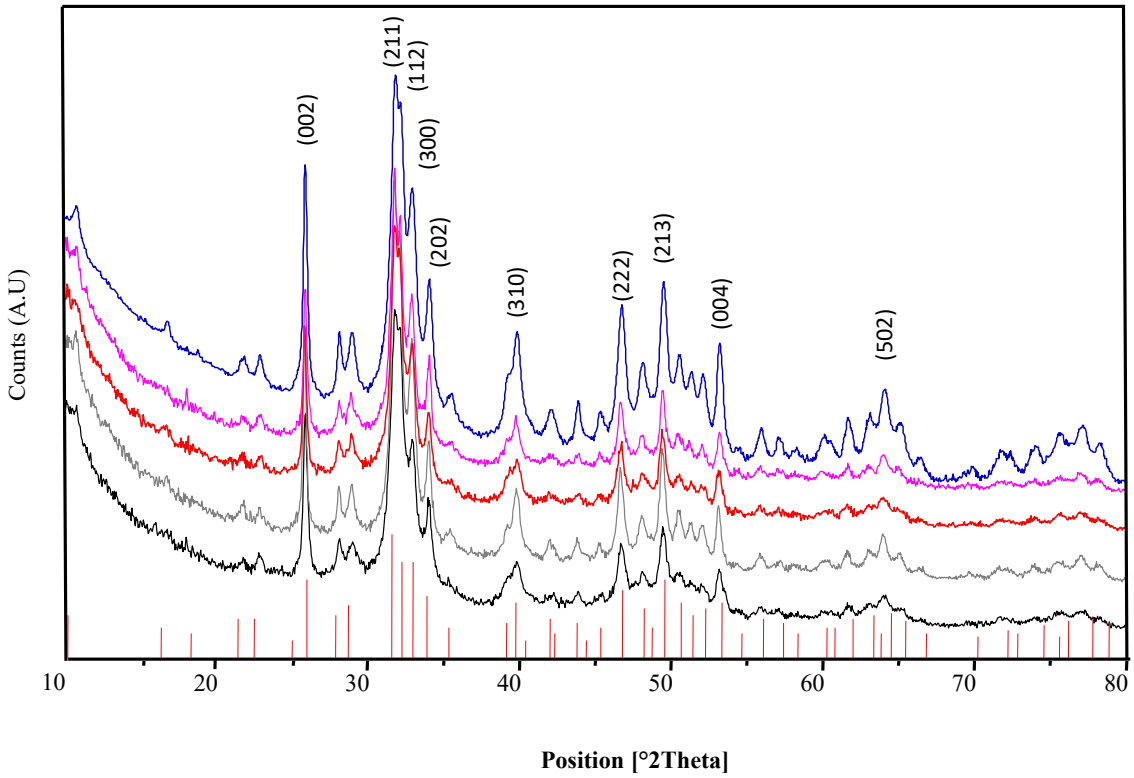

Figure 1. XRD diffraction patterns collected on (from the top to the bottom) HAp, TiHA50, TiHA25, TiHA17 and TiHA8.

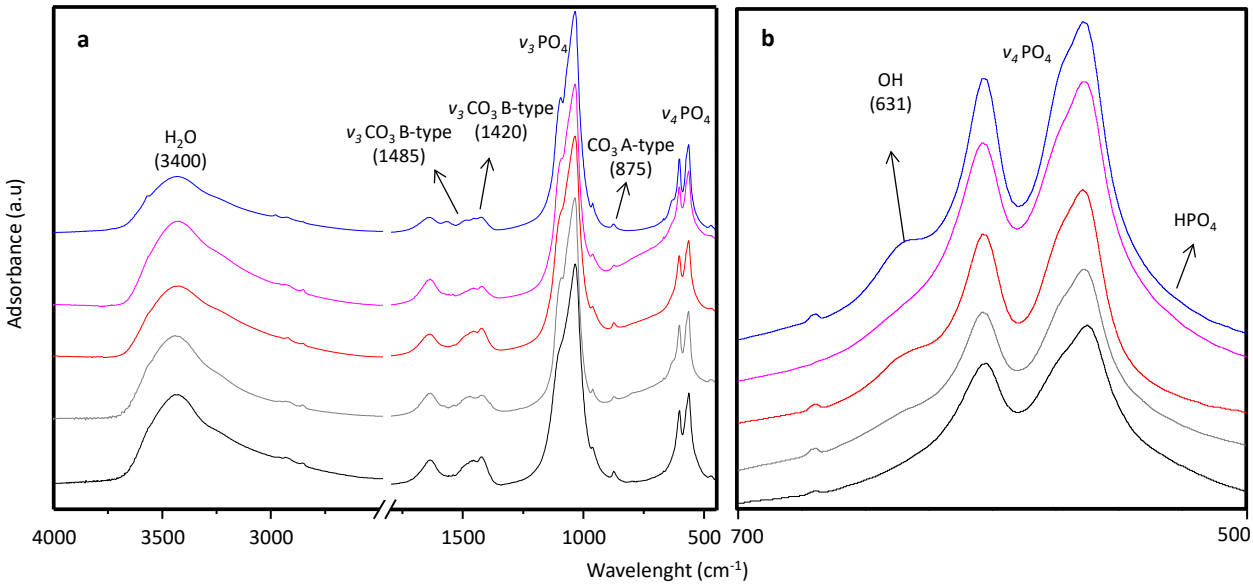

Figure 2. FT-IR spectra of (from the top to the bottom) HAp, TiHA50, TiHA25, TiHA17 and TiHA8 (a). Magnification of the FT-IR spectra in the region where the bands of ν_4PO_4 (675–525 cm^{-1}) appeared (b).

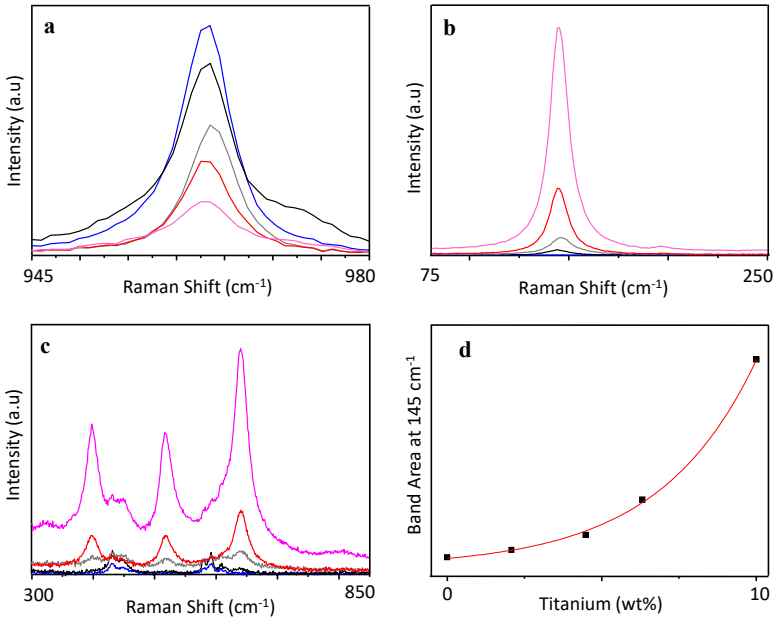

Figure 3. Evolution of the Raman bands of apatite (3a) and anatase (3b and 3c) of thermally treated HAp (blue), TiHA8 (black), TiHA17 (grey), TiHA25 (red), and TiHA50 (violet), together with the curve obtained by plotting the area of the Raman band at 145 cm^{-1} registered on all the TiHAs as a function of their Ti concentration (3d).

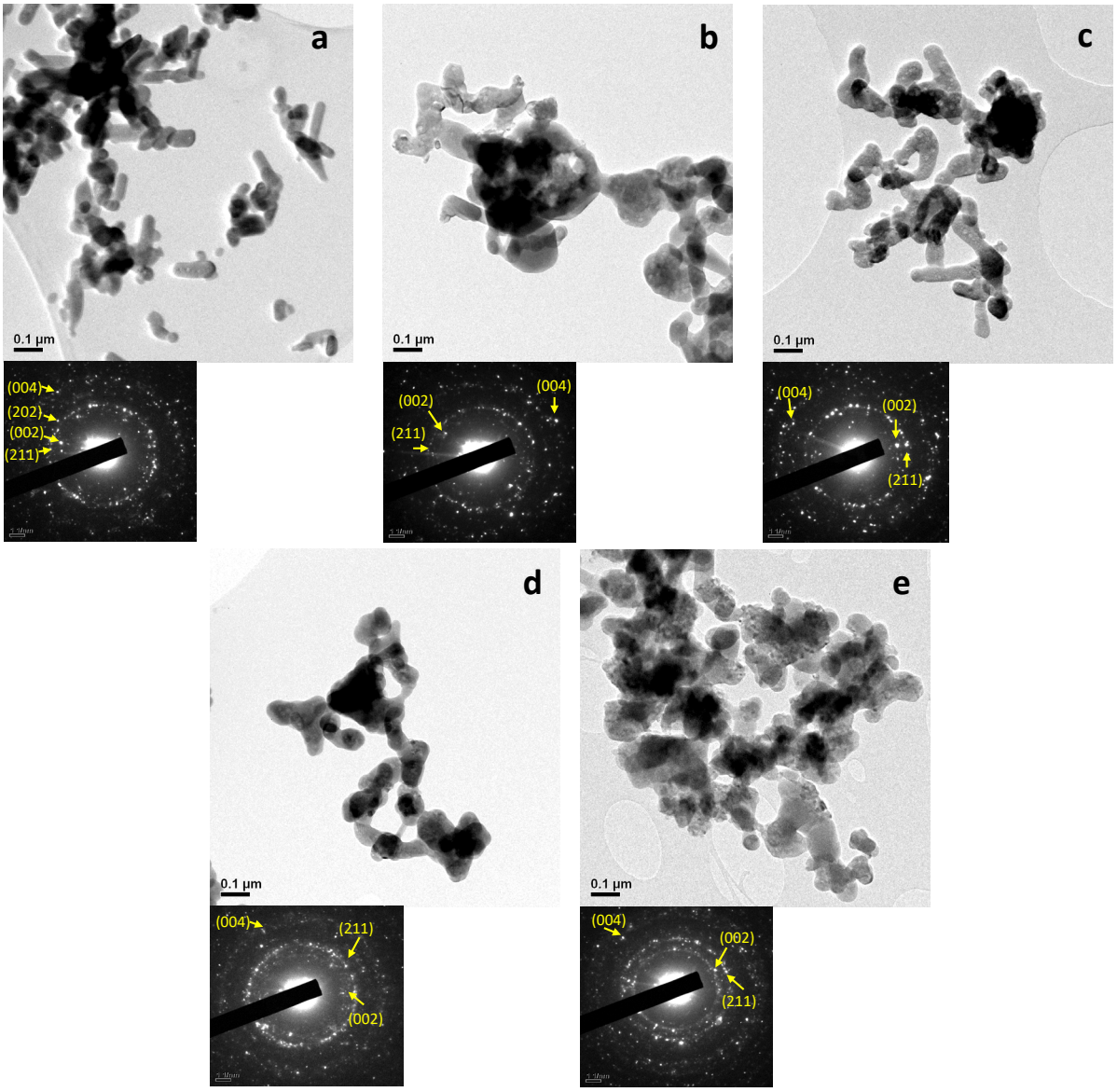

Figure 4. TEM pictures and SAED patterns collected on samples HAp (a) TiHA8 (b) TiHA17 (c) TiHA25 (d) and TiHA50 (e).

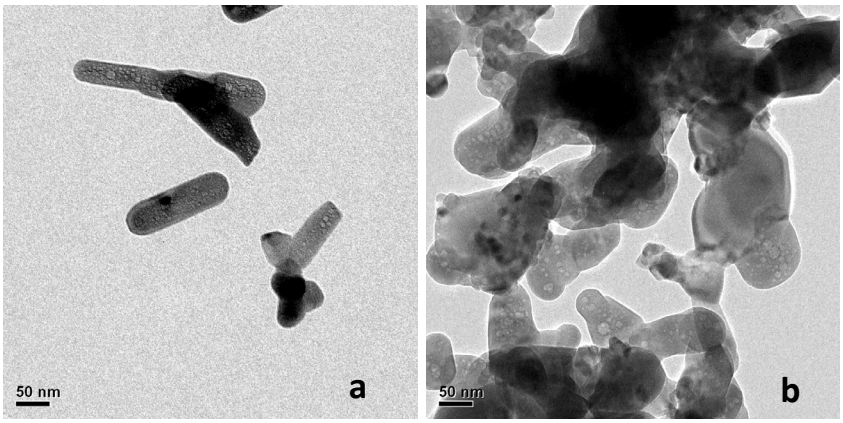

Figure 5. TEM pictures of HAp (a) and TiHA (b) at high magnification showing NPs nanopores.

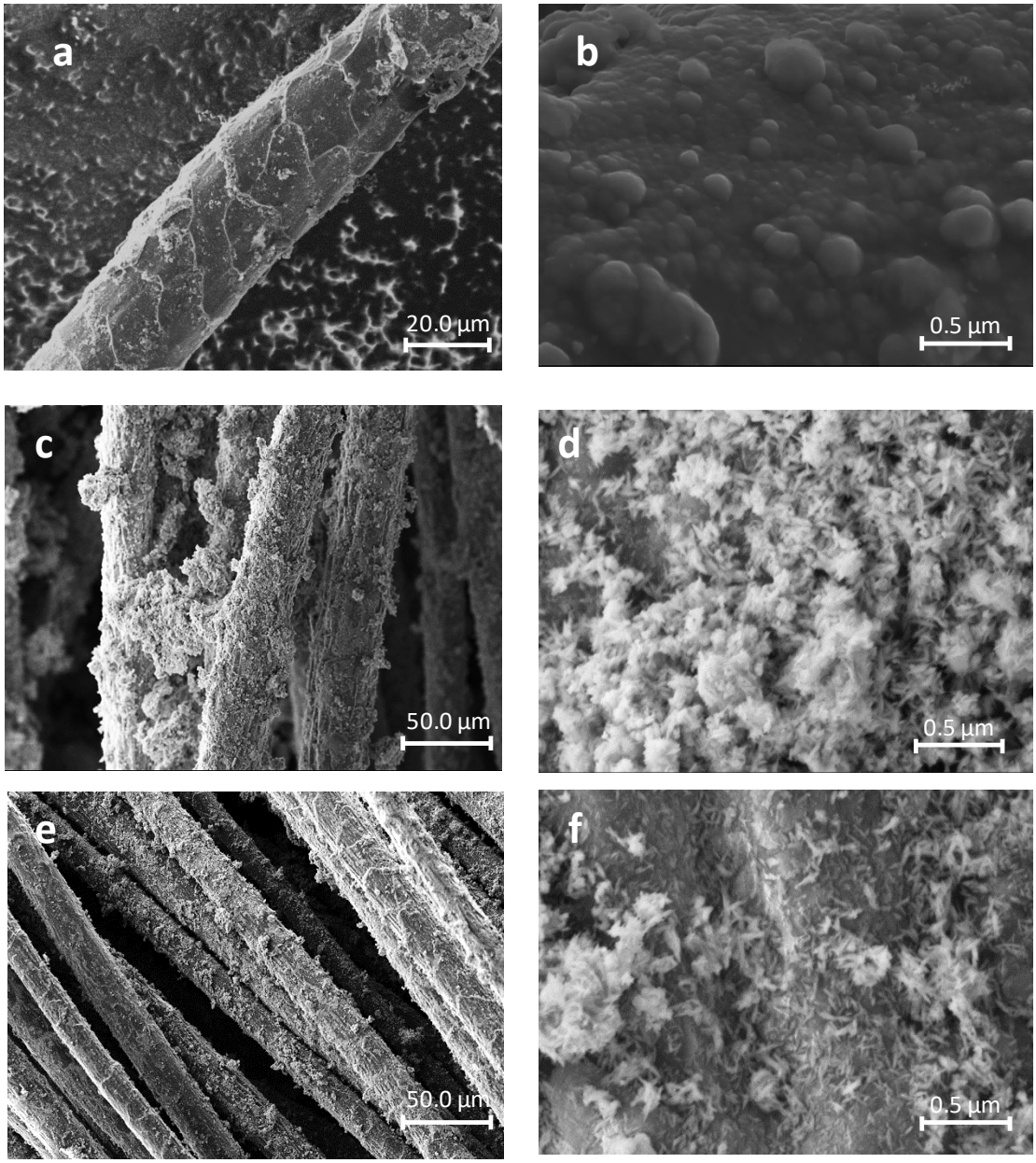

Figure 6. SEM pictures of wool fibers coated by PPy mineralized with TiHA25. Surface of the WAP fibers after mineralization at increasing magnification (a,b); Surface of the WEAP5(c,d) and WEAP10 (e,f) fibers after mineralization at increasing magnification

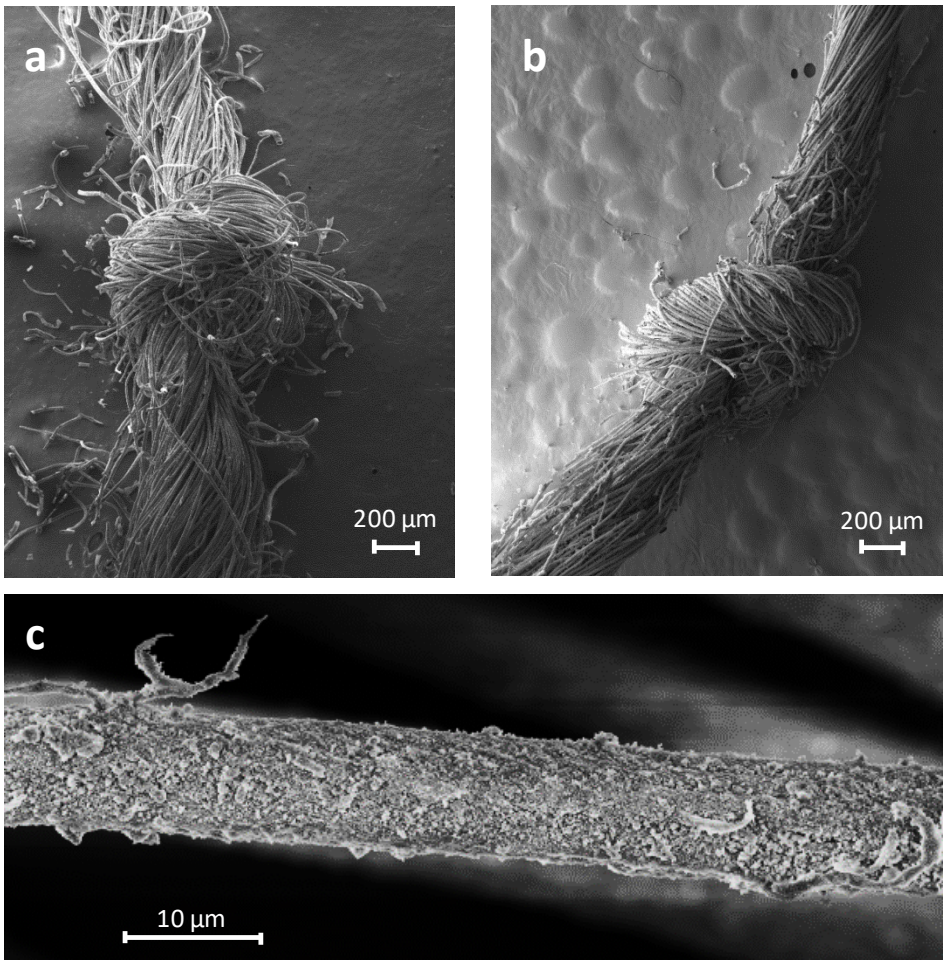

Figure 7. SEM pictures of knotted WEAP5 yarns before (a) and after (b) bio-inspired mineralization, with a micrography of mineralized WEAP5 after dipping at 40°C in ethanol for 15 minutes (c).

Table 1. Cell parameters calculated by Rietveld analysis of the XRD spectra reported in Fig.1. Cristallinity degree was calculated applying the formula described in eqn(1)[a]. Standard deviation is < 1%.

	HA	**TiHA8**	**TiHA17**	**TiHA25**	**TiHA50**
a (Å)	9,424	9.425	9.427	9.427	9.441
c (Å)	6,884	6.889	6.894	6.892	6.889

V(Å^3)	529,5	529.9	530.5	530.4	531.7
Cristallinity (%)[a]	67	64	55	54	52
IR-SF	2.06	1.24	2.02	1.52	1.63

Table 2. Phase composition determined by Rietveld refinement of the XRD spectra collected on samples treated at 700°C for 6 hours. Standard deviation is < 1%

	HAp	**TiHA8**	**TiHA17**	**TiHA25**	**TiHA50**
HA (%)	100	94,5	74,2	75,7	67,4
b-TCP (%)	0	5,5	23,3	15,3	17,5
TiO_2 (an) (%)	0	0	2,5	9,0	15,1

Table 3. Chemical composition of synthesized HAs determined by ICP-OES, together with carbonation determined by TGA and specific surface area determined by BET. Values are an average of 3 analysis. Error is reported as standard deviation

	HA	**TiHA8**	**TiHA17**	**Ti-HA25**	**TiHA50**
Ca wt.%	36.74 ± 0.14	37.91 ± 0.56	36.97 ± 0.33	32.21 ± 0.26	28.08 ± 0.40
P wt.%	15.09 ± 0.07	16.64 ± 0.08	14.59 ± 0.10	14.05 ± 0.06	12.24 ± 0.06
Ti wt.%	-	2.08 ± 0.01	4.48 ± 0.04	6.32 ± 0.03	10.01 ± 0.1
[a]CO_2 wt.% [a]	1.46 ± 0.07	1.61 ± 0.08	1.80 ± 0.09	1.72 ± 0.12	1.57 ± 0.08
Ca/P molar	1.69 ± 0.03	1.76 ± 0.03	1.96 ± 0.07	1.77 ± 0.04	1.77 ± 0.05
(Ti+Ca)/P molar	-	1.84 ± 0.03	2.16 ± 0.06	2.06 ± 0.03	2.30 ± 0.04
Ca/(P+Ti) molar	-	1.65±0.05	1.64±0.05	1.38±0.06	1.16±0.05
Ti/P molar	-	7.66±0.40	16.95±0.85	27.42±0.91	49.83±1.00

[b]***SSA m²/g***	84±9	101 ± 10	123 ± 12	146 ± 13	134 ± 13

[a] Determined by TGA
[b] Determined by BET